A Variable Stiffness PZT Actuator Having Tunable Resonant Frequencies

A Variable Stiffness PZT Actuator Having Tunable Resonant Frequencies

Thomas W. Secord, *Student Member, IEEE*, and H. Harry Asada, *Member, IEEE*

***Abstract*—A new approach to a variable stiffness actuator with tunable resonant frequencies is presented in this paper. Variable stiffness actuators have become increasingly important to meet safety requirements and achieve adaptive manipulation or locomotion. For cyclic motion, exploiting dynamic resonance can lead to high power transmission, high energy efficiency, and large motion amplitude. Resonance and variable stiffness characteristics have yet to be incorporated into a single actuator design. In this paper, a cellular artificial muscle actuator that achieves both variable stiffness and variable resonance capabilities is presented. The design is based on piezoelectric stack actuators. First, the principle of variable stiffness and variable resonant frequencies is described. The static and dynamic performance are then quantified with theoretical models. Theoretical analysis reveals that the proposed actuator can be tuned over a broad range of resonant frequencies by selectively turning specific units ON or OFF. Initial prototypes are tested experimentally and exhibit 15% static strain, over 300% static stiffness tunability, and over 100% dynamic resonance tunability.**

***Index Terms*—Actuators, piezoelectric actuators, resonance, tunable devices.**

I. Introduction

VARIABLE stiffness actuators have the capability to meet the increased demand for safety, robust locomotion, and dynamic manipulation. In robots interacting with humans, variable stiffness actuators allow maximum forces to be held to acceptable levels [1]. In mobile robots, joint compliance absorbs impulsive forces from the ground and allows a vehicle to negotiate better on rough terrain. Actuator compliance is also essential to manipulate objects in unstructured environments, where the properties of the manipulated object are not known *a priori*. Although feedback control is one way of varying task space stiffness [2], the bandwidth of the control loop is usually insufficient for rapid and highly dynamic physical interaction. Therefore, it is desirable to have variable mechanical compliance inherent in the actuator's physical construction.

Several groups have investigated both constant stiffness and variable stiffness actuators. In the early work on the elastic hand [3] and [4], elastic elements were inserted in an actuator drive train for stable grasping and dexterous manipulation. The seminal work of Pratt and Williamson [5] demonstrated the advantages of constant series elasticity to increase shock tolerance, reduce reflected inertia, and improve force control. These concepts are still employed in current systems, such as advanced protheses that utilize both series and parallel elasticity to enhance force bandwidth [6]. Although constant stiffness in a drive train is beneficial, additional advantages are obtained when the stiffness is allowed to vary. A majority of the work in variable stiffness actuators has been directed to develop new variable stiffness rotary joints. For example, in [7], the stiffness of a joint is varied by changing the overlapping area of two permanent magnets. In [1], a combined spring and belt-drive system achieves variable stiffness. Contemporary designs using similar ideas were proposed in [8] and [9]. A theme among these actuator designs is the requirement of two actuators for a single degrees of freedom (DOF). Moreover, all the designs employ standard electromechanical actuators: One actuator allows for stiffness tunability and another for angular motion.

In the context of robotics, resonance is often addressed separately from tunable resonance. Resonance is a condition exhibited by linear (and weakly nonlinear) systems and is a manifestation of maximal potential and maximal kinetic energy oscillating 180° out of phase. For multi-DOF systems, this condition can occur at multiple frequencies. The frequencies, where resonance occurs depend upon the distribution of mass and stiffness within the oscillatory system. In robotics, resonance has been recognized as an important phenomenon that can be used to increase power transmission to a load, reduce the effort of actuators, and achieve a large amplitude motion for cyclic tasks, such as running (e.g., [10], [11]), flapping (e.g., [12], [13]), or fin-based swimming (e.g., [14]).

Variable stiffness and resonance can be intimately connected because the ability to vary actuator stiffness provides the ability to tune a robotic system's resonant frequencies. Indeed, some recent work has simulated tunable stiffness as a means for tuning resonant-like frequencies in multi-DOF manipulators [15]. Other work in actuator design has considered the constant resonant frequencies in certain material systems such as piezoelectric (PZT) beam actuators [16] and electrostrictive polymers [17]. Because of the great importance of both variable stiffness and tunable resonance, there exists a need for an actuator that can provide both functions.

This paper presents the design, analysis, and testing of a new linear artificial muscle actuator that incorporates both variable stiffness and tunable resonant frequencies by using a modular, cellular architecture. Artificial muscle actuator design is

Manuscript received August 7, 2009; revised March 1, 2010 and July 25, 2010; accepted September 6, 2010. Date of publication November 1, 2010; date of current version December 8, 2010. This paper was recommended for publication by Associate Editor A. Albu-Schäffer and Editor K. Lynch upon evaluation of the reviewers' comments.

T. W. Secord is with d'Arbeloff Laboratory, Massachusetts Institute of Technology, Cambridge, MA 02139 USA (e-mail: secord@mit.edu).

H. H. Asada is with the Department of Mechanical Engineering, Massachusetts Institute of Technology, Cambridge, MA 02139 USA (e-mail: asada@mit.edu).

Color versions of one or more of the figures in this paper are available online at http://ieeexplore.ieee.org.

Digital Object Identifier 10.1109/TRO.2010.2076850

considered because of its importance to many areas of biorobotics that require smooth and natural motions that cannot be achieved with either linear or rotary electromechanical actuators. The basic principle of the actuator design is to connect a plurality of actuator cells in series or parallel (as in natural muscle) and, then, control stiffness and resonance by turning units ON to increase compliance and OFF to reduce compliance. The distribution of stiff versus compliant units within the actuator also determines the mass distribution and, thereby, allows the resonance properties to be tuned. The cellular architecture discussed in this paper has been successfully applied by the authors' group (e.g., [18] and [19]) and is extended here to include variable stiffness and resonance.

The early conference publications on this work [20] and [21] had initial theoretical results and only limited experimental validation. This paper presents the complete theoretical analysis on tunable resonant frequencies and new experiments using an improved prototype.

This paper first presents the conceptual design and method for varying stiffness in a cellular actuator based on discrete, PZT actuator units. In Section II, the effect of distributed mass in the actuator is then taken into account, which leads to tunable resonant frequencies. The properties and ranges for tuning resonant frequencies are rigorously established using an idealized analytical model. For experimental comparison and design, the idealized model is extended to include realistic parasitic effects, such as damping. Finally, the actuator is experimentally tested.

II. Cellular Architecture and Variable Stiffness Design

This section summarizes basic principles of variable stiffness cellular actuators (VSCAs). Any VSCA implementation must possess two fundamental characteristics: 1) Cellular units that have discrete stiffness states that can be selectively switched ON or ON; and 2) Cellular units that are connected to form an aggregate output. Within this framework, many implementations are possible. For clarity, a particular PZT-based design will be described, yet the basic principles of VSCAs are applicable to a large class of cellular actuators using other smart materials and structures.

A. PZT Cellular Actuators With Large Strain Amplification

Fig. 1 shows the design concept for a nested-flexure PZT cellular actuator. Each cellular unit consists of a PZT stack and a special strain-amplification flexure called a double-layer nested flexure. This mechanism consists of an inner and outer flexure that amplify displacement by a combined factor of 20. This large amplification gain of the nested-flexure system is necessary because PZT has very small inherent strain (i.e., 0.1%).

Fig. 1(a) shows the planar views of the cell design. From Fig. 1(a), it is observed that as a voltage is applied to the PZT stacks, the first-layer flexure is pushed outward along thebreak Y-direction, which results in an outward amplified displacement in the Z-direction provided that the underformed beam angle θ_1 is small. The second-layer flexure is then pushed outward in the Z-direction by the first layer, which results in a further amplified

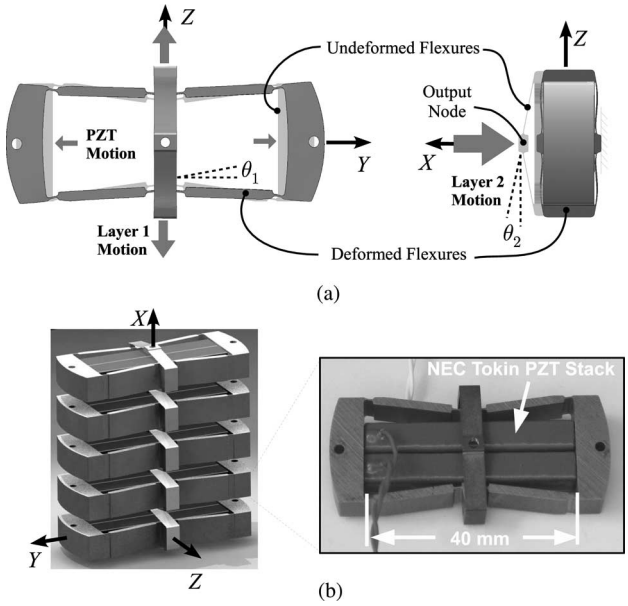

Fig. 1. (a) Working principle showing deformed and undeformed flexures in two planes. (b) Five-cell artificial muscle actuator based on PZT-driven flexures. The physical prototype uses two NEC Tokin PZT stacks.

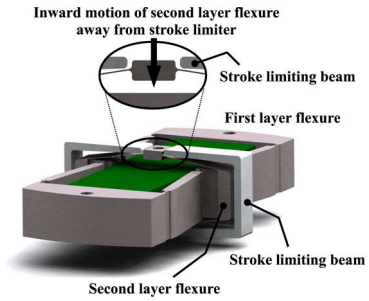

Fig. 2. Design of a variable stiffness PZT-based cell. The system consists of two strain amplification layers. The second-layer flexure incorporates a stroke-limiting beam.

displacement in the inward X-direction, when $\theta_2 \ll 1$. Therefore, a contraction force is generated along the X-axis output as the PZT stacks are activated. This contractile double-layer flexure design provides motion along the X-axis and allows the connection of multiple units in series without buckling of the flexures. The system exhibits small friction, natural axial compliance, and backdriveability. A thorough description of the actuator operating principle can be found in [22].

A serial connection of five cells is shown in Fig. 1(b), where each prototype cell shown to the right has a 20-N blocking force and 1.5 mm free displacement (which is approximately 15% of its body length along the X-axis output). The five-cell serial connection then produces 7.5 mm free displacement.

B. Variable Stiffness Mechanism

Fig. 2 shows a modification to the design in Fig. 1 to achieve variable stiffness. Outside the second-layer flexure is a rigid structure that limits the stroke of the output displacement in the Y-direction. When the PZT is not activated, the output node

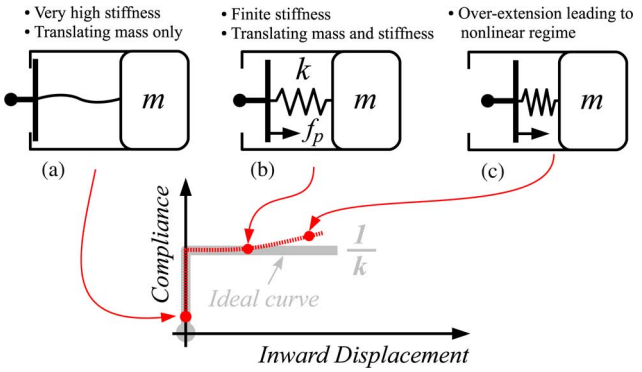

Fig. 3. Compliance versus displacement characteristics and schematic representations for a variable stiffness. PZT-actuated cell. (a) Cell in the OFF state. (b) Cell in the ON state and linear regime. (c) Cell in the ON state and nonlinear regime.

of the second-layer flexure rests on the stroke-limiting beam. The output node movement is also limited when an excessive tensile force acts on the output node. As the applied PZT voltage increases, the output node is pulled inward and is detached from the stroke-limiting beam.

Fig. 3 shows the displacement versus compliance characteristics for a single cell and corresponding schematic representations of a cell at various points along the operating curve. In the schematic representations (a)–(c), the outermost thin lines indicate the stroke limiter, while the vertical thick line represents the output node of the flexure. The schematics show all of the stiffness within the cell lumped into a single element with a constant value k. Similarly, all of the mass of a cell is lumped into a single mass element m, and damping effects are neglected to simplify the initial analysis.

As the PZT-induced force f_p increases, inward displacement also increases and the thick vertical line detaches from the limiter. For the ideal cell, the equivalent compliance seen at the output node is $1/k$. The nonlinearity in the actual compliance curve occurs because of the geometric nonlinearity of the flexure that becomes more pronounced as the cell contracts. The nonlinearity is often negligible during typical operation of the PZT-based system.

Note that it is also possible to design the stroke-limiting system so that the stroke is limited only after the maximum contraction is achieved. This would provide a compliance characteristic that drops to zero upon achieving maximum contraction. Such a cell would be actively OFF and passively ON rather than actively ON and passively OFF. For brevity, this paper only consider cells that are actively ON and passively OFF.

C. Serial, Parallel, and Antagonistic Connections

The aforementioned cellular units can be connected in series, parallel, or antagonistic configurations, creating diverse stiffness characteristics as a collective sum. The most fundamental VSCA is a serial connection of N units. This arrangement is referred to as a strand. For simplicity, assume that the stiffness of an OFF state unit is infinitely large, while stiffness in the ON state is a constant k. If n units are ON and the others are OFF, then the

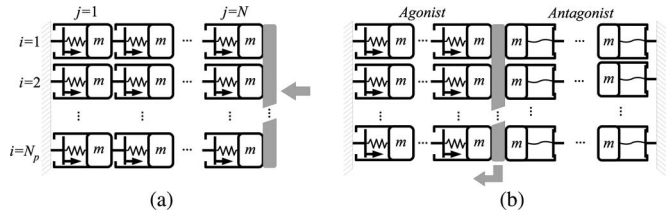

Fig. 4. (a) Parallel arrangement of cellular units. Note that one end of the actuator is shown connected to ground only for clarity, but myriad other boundary conditions are possible. (b) Antagonistic pairing of actuator strands.

resultant stiffness of an N-unit strand reduces to

$$k_S = \frac{k}{n}, \quad 1 \leq n \leq N. \tag{1}$$

Next, consider a parallel arrangement of strands. As shown in Fig. 4(a), N_p strands of N serially connected units may be arranged in parallel. If the ith strand of serially connected units has stiffness $k_{S,i}$, the resultant stiffness of the entire system is given by

$$k_P = \sum_{i=1}^{N_p} k_{S,i}. \tag{2}$$

To accommodate the stiffness to a desired value, one can determine the number of parallel strands N_p and the number of ON units n_i in each strand of serial units.

The N_p strands can be divided into two sets of strands to form an agonist–antagonist arrangement, as shown in Fig. 4(b). Both the agonist and antagonist strands contribute to an output stiffness as a direct sum: $k_{\text{out}} = k_{P,\text{ag}} + k_{P,\text{an}}$. The antagonistic arrangement allows for varying stiffness independent of position, as in the case of natural skeletal muscles [23]. However, unlike skeletal muscles, the stiffness seen at the output of a VSCA will decrease as more cells are activated. Therefore, the limitation of the VSCA technique is that large displacements and large stiffness cannot be obtained simultaneously because many units must be in the ON (compliant) state to accommodate large displacements.

III. Tunable Resonant Frequencies

A. Principle

As demonstrated for varying stiffness, the resonant frequencies of a collection of cellular units can also be varied by exploiting the cellular architecture. The key behavior is that turning on a specific number of units to achieve a desired static stiffness still allows for numerous ON–OFF unit combinations, each of which exhibits different vibration modes with different resonant frequencies. Although the total number of ON state units remains the same, the resonant frequencies may vary significantly depending upon the location of the ON units within the actuator.

To illustrate the basic concept, recall the simplified dynamic model shown in Fig. 3. Consider three of these units connected serially. Suppose that two out of the three units are turned ON so that the static stiffness of the serial connection is $k_S = k/2$.

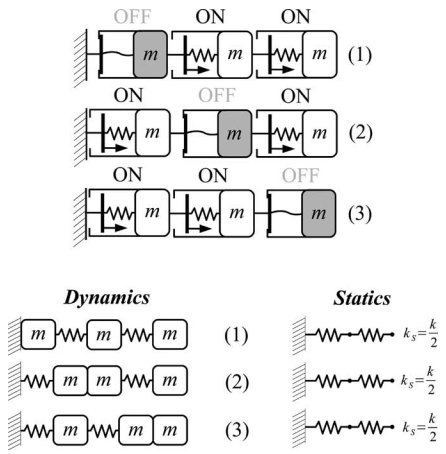

Fig. 5. Comparison of static and dynamic behavior for all possible ON–OFF distributions for three serially connected units having two units activated.

TABLE I
FIRST AND SECOND NATURAL FREQUENCIES OF EACH OF THE THREE CONFIGURATIONS

Configuration	$\frac{\omega_1}{\sqrt{k/m}}$	$\frac{\omega_2}{\sqrt{k/m}}$
1) OFF-ON-ON	0.62	1.62
2) ON-OFF-ON	0.54	1.31
3) ON-ON-OFF	0.47	1.51

There are three unique ways to select two units to turn ON, and they are shown in the upper portion of Fig. 5. Depending upon which two units are ON, the assembly dynamic behavior is different, while the static behavior is the same.

Since all of the actuator configurations in Fig. 5 have two DOF, each configuration has two distinct vibration modes with distinct resonant frequencies. Table I shows the normalized resonant frequencies for each of the three ON–OFF states having $n = 2$. The second mode of configuration (1) OFF–ON–ON provides the highest resonant frequency overall ($1.62\sqrt{k/m}$), while the lowest resonant frequency ($0.47\sqrt{k/m}$) occurs for the first mode of the ON–ON–OFF configuration. In each case, the OFF-unit mass creates a different dynamic system and, thereby, changes the resonant frequencies.

Since all three cases have the same static stiffness k_S, but different resonance properties, this example demonstrates that actuator stiffness and resonant frequencies can be independently changed. Although the resonant frequencies do not vary continuously, multiple choices are available for different task requirements and, as the number of cellular units increases, the number of possible stiffness levels and resonant frequencies also increases. The next section establishes the model to determine resonant frequency bounds of N serially connected units.

B. Basic Model of Serial Connection Dynamics

Consider a single serially connected strand of N cellular units. Suppose that n units are in ON state so that n springs are detached from the stroke limiters. This creates an n-DOF system with each DOF corresponding to a single lumped mass that moves independently along a single axis. This means that $(N - n)$ OFF-state units are rigidly connected to other units, as illustrated in Fig 6. Let x_i be the position of the ith combined masses and $\mathbf{x}$ be a vector collectively representing the n lumped-mass displacements: $\mathbf{x} = [x_1, x_2, \ldots, x_n]^T$.

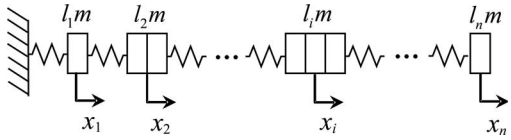

Fig. 6. Idealized dynamic model for an N-unit strand of cells having n units activated.

The ith lumped mass consists of l_i cellular units with total mass of $l_i m$ with $l_i \in \mathbb{N}$. From Fig. 6, the equations of unforced motion are obtained as follows:

$$l_i m\ddot{x}_i = -2kx_i + kx_{i-1} + kx_{i+1}, \qquad 2 \le i \le n-1 \quad (3)$$

and for $i = 1$ and $i = n$

$$l_1 m\ddot{x}_1 = -2kx_1 + kx_2, \qquad l_n m\ddot{x}_n = -kx_n + kx_{n-1}. \quad (4)$$

These equations can be arranged into vector–matrix form

$$\mathbf{M}\ddot{\mathbf{x}} + \mathbf{K}\mathbf{x} = \mathbf{0} \quad (5)$$

where $\mathbf{M} = m \cdot \text{diag}(l_1, l_2, \ldots, l_n) \triangleq m\mathbf{L}$, and

$$\mathbf{K} = k \begin{pmatrix} 2 & -1 & & 0 \\ -1 & 2 & \ddots & \\ & \ddots & 2 & -1 \\ 0 & & -1 & 1 \end{pmatrix} \triangleq k \cdot \mathbf{S}. \quad (6)$$

One important assumption of the model is that the longitudinal vibrations in a strand are the dominant dynamic behavior for the actuator. This assumption will be addressed in the practical system through an application of preload tension, as discussed in Section V.

C. Maximum and Minimum Resonant Frequencies for a Specified Static Stiffness

The model developed in Section II-C can now be utilized to determine how widely the resonant frequencies can be tuned, while satisfying the static stiffness requirement, i.e., a specified number of ON units n. For the model in (5), the squared resonant frequencies of the n-DOF mass–spring system are given by the eigenvalues of matrix product $\mathbf{M}^{-1}\mathbf{K}$

$$\omega_i^2 = \lambda_i(\mathbf{M}^{-1}\mathbf{K}) = \frac{k}{m}\lambda_i(\mathbf{L}^{-1}\mathbf{S}), \qquad 1 \le i \le n. \quad (7)$$

The n eigenvalues of the matrix are ordered from the minimum to the maximum and written as follows:

$$\lambda_{\min}(\mathbf{M}^{-1}\mathbf{K}) \le \lambda_2(\mathbf{M}^{-1}\mathbf{K}) \le \cdots \le \lambda_{\max}(\mathbf{M}^{-1}\mathbf{K}). \quad (8)$$

For a fixed number of ON-state units n, the stiffness matrix $\mathbf{K}$ remains the same regardless of the arrangement of ON–OFF units. The mass matrix $\mathbf{M}$ on the other hand, varies depending on the ON–OFF arrangement within the strand. Therefore, the aforementioned $\lambda_{\min}(\lambda_{\max})$ can be further decreased (increased) by changing the ON–OFF unit configurations, thereby changing the mass matrix.

Given a specific static stiffness k_S, which will uniquely determine n, consider the set of all mass matrices associated with the possible distributions of N cells into n clusters of masses

$$\mathfrak{M}_n = \left\{ \mathbf{M} = m \cdot \mathrm{diag}(l_1, \ldots, l_n) \,\middle|\, \sum_{i=1}^{n} l_i = N - p \right. \\ \left. p = 0, \ldots, N-n;\ l_i \in \mathbb{N} \right\}, \quad n = 1, 2, \ldots, N. \tag{9}$$

The number of possible arrangements of n ON units within a strand is equivalent to the cardinality of $\mathfrak{M}_n$ and is $\binom{N}{n}$.

If the first p units are turned OFF, then they become fixed to the base structure and do not participate in the dynamics. With p units OFF at the base, the total number of ON units is then $(N-p)$, where p can take on values $1, 2, \ldots, (N-n)$. Thus, the subset of $\mathfrak{M}_n$, which is defined by $p = 0$ in (9), is the set of all possible mass matrices assuming that the first unit in the strand is in the ON state so that all cell masses are dynamically participating.

Let $\sigma_{\min}(n)$ be the minimum of the positive square root of $\lambda_{\min}(\mathbf{M}^{-1}\mathbf{K})$ with respect to all $\mathbf{M} \in \mathfrak{M}_n$

$$\sigma^2_{\min}(n) = \min_{\mathbf{M} \in \mathfrak{M}_n} \lambda_{\min}(\mathbf{M}^{-1}\mathbf{K}). \tag{10}$$

$\sigma_{\min}(n)$ provides the lowest resonant frequency among all the ON–OFF unit distributions having n ON-state units.

Recall that the minimum eigenvalue of $\mathbf{M}^{-1}\mathbf{K}$ is given by the minimum of the Rayleigh quotient

$$\lambda_{\min}(\mathbf{M}^{-1}\mathbf{K}) = \min_{\mathbf{x} \in \mathbb{R}^n} \frac{\mathbf{x}^T\mathbf{K}\mathbf{x}}{\mathbf{x}^T\mathbf{M}\mathbf{x}}. \tag{11}$$

Similarly, the highest resonant frequency is given by

$$\sigma^2_{\max}(n) = \max_{\mathbf{M} \in \mathfrak{M}_n} \lambda_{\max}(\mathbf{M}^{-1}\mathbf{K}) \\ = \max_{\mathbf{M} \in \mathfrak{M}_n} \left(\max_{\mathbf{x} \in \mathbb{R}^n} \frac{\mathbf{x}^T\mathbf{K}\mathbf{x}}{\mathbf{x}^T\mathbf{M}\mathbf{x}} \right). \tag{12}$$

Using (12), one can prove the following proposition concerning the highest resonant frequency $\sigma_{\max}(n)$ and the ON–OFF unit distribution that provides $\sigma_{\max}(n)$.

Proposition 1: Let $\mathbf{M} = m\mathbf{L}$ and $\mathbf{K} = k\mathbf{S}$ be, respectively, the $n \times n$ mass and stiffness matrices of N serially-connected cellular units among which n units are active (turned ON). The highest resonant frequency occurs when the first $N-n$ units are turned OFF. This maximum frequency is given by

$$\sigma_{\max}(n) = \sqrt{\frac{k}{m}\lambda_{\max}(\mathbf{S})}. \tag{13}$$

Proof: Since $\mathbf{x}^T\mathbf{M}\mathbf{x} \geq m\mathbf{x}^T\mathbf{I}\mathbf{x}\ \forall \mathbf{M} \in \mathfrak{M}_n$ and $\forall \mathbf{x} \in \mathbb{R}^n$

$$\lambda_{\max}(\mathbf{M}^{-1}\mathbf{K}) = \max_{\mathbf{x} \in \mathbb{R}^n} \frac{\mathbf{x}^T\mathbf{K}\mathbf{x}}{\mathbf{x}^T\mathbf{M}\mathbf{x}} \\ \leq \max_{\mathbf{x} \in \mathbb{R}^n} \frac{k\mathbf{x}^T\mathbf{S}\mathbf{x}}{m\,\mathbf{x}^T\mathbf{I}\mathbf{x}} \\ = \frac{k}{m}\lambda_{\max}(\mathbf{S}).$$

Therefore

$$\arg\max_{\mathbf{M} \in \mathfrak{M}_n} \lambda_{\max}(\mathbf{M}^{-1}\mathbf{K}) = \mathrm{diag}(m, m, \ldots, m).$$

Hence, the arrangement where the first $(N-n)$ units are turned OFF [i.e., $p = (N-n)$ in (9)] yields $\sigma_{\max}(n)$. ■

To address the lowest possible resonant frequency configuration, first consider the following two lemmas:

Lemma 1: The fundamental mode of a fix-free vibrating system as shown in Fig. 6 has nodal displacements that satisfy $0 \leq x_1 \leq x_2 \leq \cdots \leq x_n$.

Lemma 2: Consider the scalar function defined by

$$J(l_1, l_2, \ldots, l_n) \triangleq \mathbf{x}^T\,\mathrm{diag}(l_1, l_2, \ldots, l_n)\mathbf{x} \tag{14}$$

where the l_i satisfy the conditions in (9), and the vector $\mathbf{x}$ has elements that are monotonically increasing

$$0 \leq x_1 \leq x_2 \leq \cdots \leq x_n. \tag{15}$$

The scalar function J is maximized when $l_1 = 1, l_2 = 1, \ldots, l_{n-1} = 1, l_n = N - n + 1$.

A proof of Lemma 1 can be found in [24], while a proof of Lemma 2 is given in the Appendix; both may be used in the following proposition for $\sigma_{\min}(n)$.

Proposition 2: The arrangement having all the inactive units placed at the unconstrained end of the serial connection gives the lowest undamped resonant frequency $\sigma_{\min}(n)$.

Proof: By Lemma 1, the first mode shape can be considered positive and monotonically increasing. Therefore

$$\min_{\mathbf{M} \in \mathfrak{M}_n} \frac{k\mathbf{x}^T\mathbf{S}\mathbf{x}}{\mathbf{x}^T\mathbf{M}\mathbf{x}} = \min_{\substack{\mathbf{M} \in \mathfrak{M}_n \\ 0 \leq x_1 \leq \cdots \leq x_n}} \frac{k\mathbf{x}^T\mathbf{S}\mathbf{x}}{\mathbf{x}^T\mathbf{M}\mathbf{x}} \\ = \min_{0 \leq x_1 \leq \cdots \leq x_n} \frac{k\mathbf{x}^T\mathbf{S}\mathbf{x}}{\mathbf{x}^T\mathbf{M}_0\mathbf{x}}$$

where $\mathbf{M}_0 \triangleq m \cdot \mathrm{diag}(1, 1, \ldots, N-n+1)$ by Lemma 2. This represents the case, where all of the inactive units are placed at the unconstrained end. ■

In many practical situations, the first (i.e., fundamental) mode is the most readily excited. Therefore, to establish a range for the fundamental frequency tunability, the highest value for the first resonant frequency will be given the notation $\sigma_{\max,\mathrm{first}}(n)$ and defined as follows:

$$\sigma^2_{\max,\mathrm{first}}(n) = \max_{\mathbf{M} \in \mathfrak{M}_n} \lambda_{\min}(\mathbf{M}^{-1}\mathbf{K}) \\ = \max_{\mathbf{M} \in \mathfrak{M}_n} \left(\min_{\mathbf{x} \in \mathbb{R}^n} \frac{\mathbf{x}^T\mathbf{K}\mathbf{x}}{\mathbf{x}^T\mathbf{M}\mathbf{x}} \right). \tag{16}$$

Corollary to Proposition 2: The arrangement having the first $(N-n)$ units turned OFF gives the highest possible value for the first undamped resonant frequency $\sigma_{\max,\text{first}}(n)$.

Proof: The proof follows from the proof of Proposition 1, since $\forall \mathbf{M} \in \mathfrak{M}_n$ and $\forall \mathbf{x} \in \mathbb{R}^n$, $\mathbf{x}^T\mathbf{M}\mathbf{x} \geq m\mathbf{x}^T\mathbf{I}\mathbf{x}$. Hence

$$\begin{aligned}\lambda_{\min}(\mathbf{M}^{-1}\mathbf{K}) &= \min_{\mathbf{x}\in\mathbb{R}^n} \frac{\mathbf{x}^T\mathbf{K}\mathbf{x}}{\mathbf{x}^T\mathbf{M}\mathbf{x}} \\ &\leq \min_{\mathbf{x}\in\mathbb{R}^n} \frac{k\mathbf{x}^T\mathbf{S}\mathbf{x}}{m\,\mathbf{x}^T\mathbf{I}\mathbf{x}} \\ &= \frac{k}{m}\lambda_{\min}(\mathbf{S}).\end{aligned}$$

Therefore, the same configuration as Proposition 1 gives the highest resonant frequency of the first mode. ■

D. Global Maximum and Minimum Resonant Frequencies

The aforementioned analysis provides the highest and lowest resonant frequencies for a fixed n, i.e., a given static stiffness. If instead the synthesis objective is to achieve the highest or the lowest resonant frequency regardless of the static stiffness, then the highest and lowest bounds can be further extended by considering all possible values of n varying from 1 to N.

The global minimum $\Sigma_{\min}(N)$ is then defined with an additional minimization over n

$$\begin{aligned}\Sigma^2_{\min}(N) &= \min_{1\leq n\leq N}\left\{\min_{\mathbf{M}\in\mathfrak{M}_n}\left\{\lambda_{\min}(\mathbf{M}^{-1}\mathbf{K})\right\}\right\} \\ &= \min_{1\leq n\leq N}\left\{\sigma^2_{\min}(n)\right\}. \qquad (17)\end{aligned}$$

A similar expression is obtained for the global maximum $\Sigma_{\max}(N)$. For the maximum, the following definition and lemma are required.

Definition: For the eigenvalue problem

$$\mathbf{K}\mathbf{x} = \lambda\mathbf{M}\mathbf{x} \qquad (18)$$

with $\mathbf{M}, \mathbf{K} \in \mathbb{R}^{N\times N}$, the associated rth reduced eigenvalue problem is

$$\mathbf{K}^{(r)}\mathbf{x}^{(r)} = \lambda^{(r)}\mathbf{M}^{(r)}\mathbf{x}^{(r)}, \qquad r = 0,\, 1,\, \ldots,\, N-1 \qquad (19)$$

where $\mathbf{M}^{(r)}$ and $\mathbf{K}^{(r)}$ are obtained by deleting the first r rows and first r columns in $\mathbf{M}$ and $\mathbf{K}$, respectively.

Lemma 3: The eigenvalues of the rth reduced eigenvalue problem $\lambda_i^{(r)}$, $i = 1,\, 2,\, \ldots,\, (N-r)$ and the eigenvalues of the $(r+1)$st reduced eigenvalue problem $\lambda_j^{(r+1)}$, $j = 1,\, 2,\, \ldots,\, (N-r-1)$ satisfy the following relation:

$$\begin{aligned}\lambda_1^{(r)} \leq \lambda_1^{(r+1)} \leq \lambda_2^{(r)} \leq \lambda_2^{(r+1)} \leq \cdots \\ \leq \lambda_{N-r-1}^{(r)} \leq \lambda_{N-r-1}^{(r+1)} \leq \lambda_{N-r}^{(r)}. \qquad (20)\end{aligned}$$

Lemma 3 can be proved using the technique found in [25], while a proof for the more general case of Jacobi matrices can be found in [26]. Now, the following proposition may be proved.

Proposition 3: A serial strand of *N* units takes the globally maximum resonant frequency $\Sigma_{\max}(N)$ at a configuration where all the *N* units are turned ON.

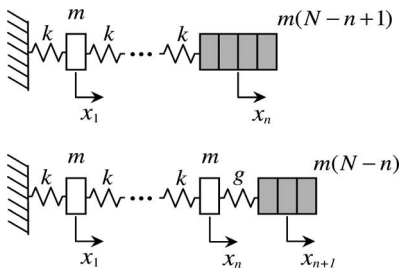

Fig. 7. Comparison of the minimum resonant frequency for the case with (top) n units ON and with (bottom) $(n+1)$ units ON.

Proof: From Proposition 1, the maximum resonant frequency for a given n, $\sigma_{\max}(n)$ occurs when the first $(N-n)$ units are turned OFF, i.e., fixed to the base structure. The associated mass matrix is given by deleting the first $(N-n)$ rows and the first $(N-n)$ columns of the $N\times N$ identity matrix multiplied by m: $m\mathbf{I}_N$. The stiffness matrix is similarly obtained by deleting the first $(N-n)$ rows and the first $(N-n)$ columns of the $N\times N$ stiffness matrix given in (6). Therefore, the global maximum of the resonant frequency can be found by comparing the largest eigenvalues of all the reduced eigenvalue problems in (19) with $r = 1,\, 2,\, \ldots,\, N-1$.

Setting $r = N-1$ in Lemma 3 gives $\lambda_1^{(N-1)} \leq \lambda_2^{(N-2)}$. Repeatedly applying Lemma 3 for $r = N-2,\, N-3,\, \ldots,\, 1$ yields

$$\lambda_1^{(N-1)} \leq \lambda_2^{(N-2)} \leq \cdots \leq \lambda_{N-1}^{(1)} \leq \lambda_N^{(0)}. \qquad (21)$$

The final eigenvalue in (21) $\lambda_N^{(0)}$ is the maximum eigenvalue of $\mathbf{M}^{-1}\mathbf{K}$ for the original $N\times N$ matrices $\mathbf{K} = k\mathbf{S}$ and $\mathbf{M} = m\mathbf{I}_N$. Therefore

$$\begin{aligned}\Sigma^2_{\max}(N) &= \lambda_{\max}\left[(m\mathbf{I}_N)^{-1}\mathbf{K}\right] \\ &= \frac{k}{m}\lambda_{\max}(\mathbf{S}) \\ &= \lambda_N^{(0)} \\ &\geq \lambda_{N-r}^{(r)}, \qquad r = 1,\, 2,\, \ldots,\, N \qquad (22)\end{aligned}$$

which concludes the proof. ■

Corollary to Proposition 3: As N increases, the globally maximum resonant frequency of an N unit strand increases monotonically

$$\Sigma_{\max}(N) \leq \Sigma_{\max}(N+1). \qquad (23)$$

Proof: Considering $\mathbf{M}$ and $\mathbf{K}$ of sufficiently large dimension and applying Lemma 3 immediately proves the corollary. ■

To obtain the global minimum $\Sigma_{\min}(N)$, recall Proposition 2. The lowest resonant frequency for a given n occurs when the last $(N-n)$ units are turned OFF, i.e., creating a lumped mass of $m(N-n+1)$ at the free end. Therefore, the question is how many units must be lumped together at the free end to minimize the resonant frequency. This can be solved by comparing the lowest eigenvalue of a strand with $(N-n)$ OFF units at the free end to the case with $(N-n-1)$ OFF units. This situation is depicted in Fig. 7.

The lower portion of Fig. 7 shows the case with $(n+1)$ units ON with a stiffness of g connecting the nth and the $(n+1)$th unit. The stiffness of g is assumed to have a lower bound value of k so that $k \leq g < \infty$. As $g \to \infty$, the vibrating system behaves as if n units are ON, and as $g \to k$, the vibrating system behaves as if $n+1$ units are ON. Using this definition of the stiffness g, it can be shown that $\sigma_{\min}(n) \geq \sigma_{\min}(n+1)$, which leads to the following proposition.

Proposition 4: A serial strand of N units takes the global minimum resonant frequency $\Sigma_{\min}(N)$ at a configuration where all the N units are turned ON.

Proof: For the $(n+1)$th order system, define the mass matrix $\mathbf{M} = m \cdot \mathrm{diag}(1,\ 1,\ \ldots,\ 1,\ N-n)$ and define the stiffness matrix $\mathbf{K}'$ as follows:

$$\mathbf{K}' = \left(\begin{array}{ccc:cc} 2k & -k & & & 0 \\ -k & \ddots & \ddots & & \\ & \ddots & 2k & -k & \\ \hdashline & & -k & k+g & -g \\ 0 & & & -g & g \end{array}\right). \tag{24}$$

The quadratic form $\mathbf{x}^T\mathbf{K}'\mathbf{x}$ can be written as two separate scalar functions

$$\mathbf{x}^T\mathbf{K}'\mathbf{x} = \Phi(x_1,\ x_2,\ \ldots,\ x_n, k) + g(x_{n+1} - x_n)^2 \tag{25}$$

where $\Phi(x_1,\ x_2,\ \ldots,\ x_n, k)$ is a positive function for any nonzero x_i with $i = 1,\ 2,\ \ldots,\ n$. Note that g is factored out in the second scalar function. Hence, $\forall \mathbf{x} \in \mathbb{R}^{n+1}$

$$\begin{aligned} \frac{\mathbf{x}^T\mathbf{K}'\mathbf{x}}{\mathbf{x}^T\mathbf{M}\mathbf{x}} &= \frac{\Phi(x_1,\ x_2,\ \ldots,\ x_n, k) + g(x_{n+1} - x_n)^2}{\mathbf{x}^T\mathbf{M}\mathbf{x}} \\ &\geq \frac{\Phi(x_1,\ x_2,\ \ldots,\ x_n, k) + k(x_{n+1} - x_n)^2}{\mathbf{x}^T\mathbf{M}\mathbf{x}} \\ &= \frac{\mathbf{x}^T\mathbf{K}\mathbf{x}}{\mathbf{x}^T\mathbf{M}\mathbf{x}}. \end{aligned} \tag{26}$$

Now let $\mathbf{x}^*$ denote the fundamental mode shape for the system having a stiffness matrix $\mathbf{K}'$. Then, using (26) and the properties of the Rayleigh quotient, it follows that

$$\begin{aligned} \lambda_{\min}(\mathbf{M}^{-1}\mathbf{K}') &= \frac{\mathbf{x}^{*T}\mathbf{K}'\mathbf{x}^*}{\mathbf{x}^{*T}\mathbf{M}\mathbf{x}^*} \\ &\geq \frac{\mathbf{x}^{*T}\mathbf{K}\mathbf{x}^*}{\mathbf{x}^{*T}\mathbf{M}\mathbf{x}^*} \\ &\geq \min_{\mathbf{x}\in\mathbb{R}^{n+1}} \frac{\mathbf{x}^T\mathbf{K}\mathbf{x}}{\mathbf{x}^T\mathbf{M}\mathbf{x}} \\ &= \lambda_{\min}(\mathbf{M}^{-1}\mathbf{K}). \end{aligned} \tag{27}$$

The aforementioned inequality shows that the case having only n units ON will have a higher fundamental frequency than the case with $n+1$ units ON because the case having only n units ON is a special case of the system with the stiffness matrix $\mathbf{K}'$ when $g \to \infty$. Therefore, $\sigma_{\min}(n) \geq \sigma_{\min}(n+1)$ for $n = 1, \ldots, N-1$, from which it immediately follows that

$$\sigma_{\min}(1) \geq \sigma_{\min}(2) \geq \cdots \geq \sigma_{\min}(N) = \Sigma_{\min}(N). \tag{28}$$

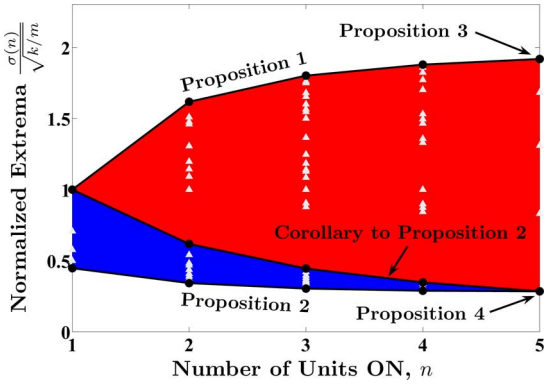

Fig. 8. Theoretical propositions for $N = 5$. All possible resonant frequencies are shown as well as numerical bounds on the minimum and maximum achievable resonant frequencies for $N = 5$.

This result shows that turning all units ON leads to the global minimum resonant frequency. ■

A numerical illustration of Propositions 1–4 is offered in Fig. 8 for $N = 5$. Fig. 8 shows the locations of all possible resonant frequencies as triangles. The maximum and minimum bounds indicated by the uppermost and lowermost solid lines are the resonant frequencies based on the configurations in Propositions 1 and 2, respectively, i.e., the uppermost points on the solid lines are achieved by placing all OFF units next to the base structure, while the lowermost points are achieved by placing all OFF units at the free end. Note that as n increases toward the maximum value of $N = 5$, the upper and lower resonant frequency bounds monotonically approach the limits specified by Propositions 3 and 4, where all units are ON. As n increases, the reduction in the absolute slope of the overall upper and lower resonance bounds implies that including more than $N \approx 5$ units in a strand does not significantly improve the range of attainable resonant frequencies, although it would increase the static stiffness tuning range.

The darker region in Fig. 8 indicates the tunable range of the first resonance only. This region's upper bound is dictated by the Corollary to Proposition 2. As given in Proposition 1, the configurations for highest first resonance have all OFF units placed at the base. The general trend of this first-mode region is a downward and narrowing behavior.

A further note regarding the theoretical resonance tunability is that there is a gap between the first mode and higher modes for $n \geq 2$. For a given n, this spacing creates a band of frequencies over which no resonance can occur. However, if all values of n are considered, the overall modal density is fairly uniform between the global limits $\Sigma_{\min}(N)$ and $\Sigma_{\max}(N)$.

E. Maximal Tuning for Long Strands

The previous propositions establish the conditions under which maximum and minimum resonant frequencies are achieved for finite N. In this section, the case, where $N \to \infty$ is considered to establish the maximal tunability using the proposed actuation method. Given an N, Propositions 3 and 4 indicate that $\Sigma_{\min}(N)$ and $\Sigma_{\max}(N)$ are given by $\sqrt{k/m}$

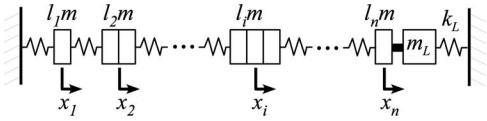

Fig. 9. Idealized dynamic model for an N-unit strand of cells rigidly connected to a spring–mass load and having n units activated.

multiplied by the positive square root of the maximum and minimum eigenvalues of $\mathbf{S} \in \mathbb{R}^{N\times N}$ having the form defined in (6). As described in [24], the eigenvalues for $\mathbf{S}$ can be written in closed form

$$\lambda_i(\mathbf{S}) = 4\sin^2\left(\frac{(2i-1)\pi}{2(2N+1)}\right), \qquad i = 1, 2, \ldots, N. \quad (29)$$

Therefore, the following two propositions bound $\Sigma_{\max}(N)$ and $\Sigma_{\min}(N)$ for all N.

Proposition 5: The maximum undamped resonant frequency $\Sigma_{\max}(N)$ has a least upper bound of $2\sqrt{\frac{k}{m}}$.

Proof: Applying (29) with $i = N$ yields

$$\Sigma_{\max}(N) = 2\sqrt{\frac{k}{m}}\sin\left(\frac{1-(1/2n)}{2+(1/N)}\pi\right). \quad (30)$$

Let us consider $N \to \infty$ gives an upper bound of $2\sqrt{k/m}$. ■

Proposition 6: The minimum undamped resonant frequency $\Sigma_{\min}(N)$ has a greatest lower bound of 0.

Proof: Applying (29) with $i = 1$ yields

$$\Sigma_{\min}(N) = 2\sqrt{\frac{k}{m}}\sin\left(\frac{1}{2(2N+1)}\pi\right). \quad (31)$$

Let us consider $N \to \infty$ gives a lower bound of 0. ■

F. Loading Effects

While the system shown in Fig. 6 possesses fixed-free boundary conditions, practical applications entail a load-end condition. A simple extension of the model in Fig. 6 is provided in Fig. 9, which shows the addition of a mass and spring load connected rigidly to the nth node. The load mass and stiffness will dictate the following dimensionless ratios:

$$\gamma_m \triangleq \frac{m_L}{m} \quad (32)$$

and

$$\gamma_k \triangleq \frac{k_L}{k}. \quad (33)$$

As $\gamma_m \to 0$ and $\gamma_k \to 0$, the system in Fig. 9 approaches the system of Fig. 6, and the theoretical conclusions in Section III-C–E apply directly. In this section, the effects of the load ratios on the static and dynamic tuning properties are considered.

The static behavior of a loaded cell strand can be classified by the tunability of the output stiffness, which will be defined as follows:

$$\%\text{Static tunability} = \left(\frac{\max(c_S) - \min(c_S)}{\min(c_S)}\right)\times 100 = \left(\frac{N-1}{1+\gamma_k N}\right)\times 100 \quad (34)$$

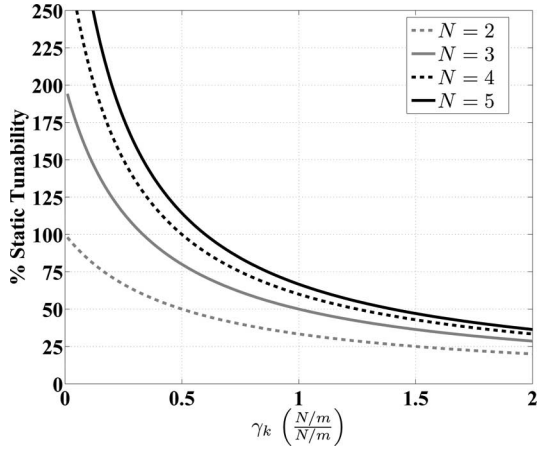

Fig. 10. Static tunability as a function of the load stiffness ratios for $N = 2$, 3, and 5.

where c_S is the equivalent compliance as viewed by forces applied at the nth node. A plot of the static tunability as a function of N and γ_k is shown in Fig. 10. Beyond $\gamma_k \approx 1.5$, the tunability drops below 50% even for the larger N values. In general, the static tunability is greatly reduced if the load stiffness exceeds approximately $0.5k$, where the curvature of the tunability curves nears its maximum.

The dynamic behavior of a strand of cells is characterized by the ability to tune resonant frequencies. The new dynamic model is the same as described previously but with $\mathbf{M} = m \cdot \text{diag}(l_1, l_2, \ldots, l_n + \gamma_m)$ and the (n, n) entry of $\mathbf{K}$ given by $k(1 + \gamma_k)$. In practical applications, the first (i.e., fundamental) mode is the most readily excited. Therefore, the tunability of the dynamic system's fundamental frequency will be defined as follows:

$$\%\text{Dynamic tunability} = \left(\frac{\sigma_{\max,\text{first}}(1) - \Sigma_{\min}}{\Sigma_{\min}}\right)\times 100. \quad (35)$$

A plot of (35) is provided in Fig. 11 for $N = 2$ to 5. Fig. 11 shows that the tunability decreases as γ_m and γ_k increase. However, for low values of γ_k, increasing γ_m has a very weak effect on tunability. Likewise, for low γ_m, the tunability is only a weak function of γ_k. The dynamic tunability also increases as N is increases. Overall, the frequency spacing between possible fundamental modes decreases as the stiffness and mass of the load increase or as N decreases.

Based on numerical evaluation, the propositions previously described remain valid except under the condition when $N = 2$ and $\gamma_k = \gamma_m + 1$. In this case, the configuration having $n = 1$ unit ON with the first unit remaining OFF (i.e., grounded) and the case having $n = N = 2$ (i.e., all units ON) both achieve a minimum fundamental frequency of $\Sigma_{\min} = \sqrt{k/m}$. Overall, the loading effects illustrate that this cellular tuning method is most effective when N is large and the actuator is scaled such that γ_k and γ_m remain within the high tunability regions of Fig. 11.

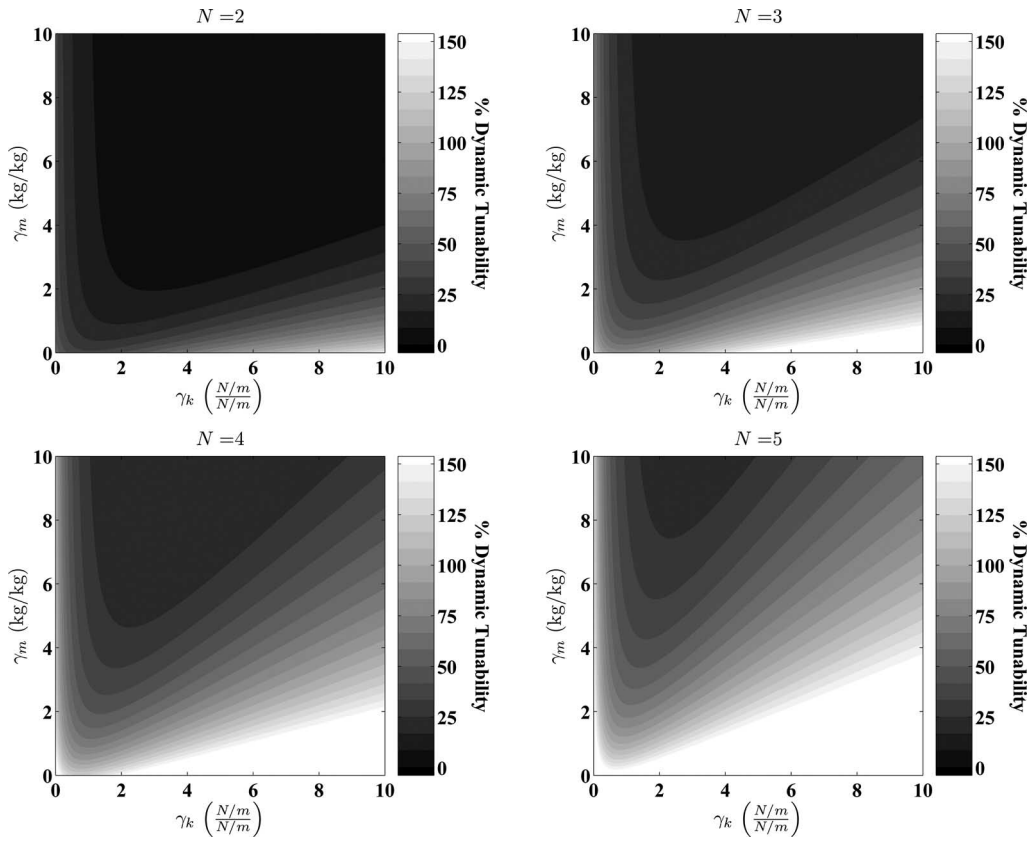

Fig. 11. Fundamental frequency tunability as a function of the load stiffness and mass ratios for $N = 2, 3, 4$, and 5.

IV. Implementation of a Piezoelectric-Based Variable Stiffness Cellular Actuator

The analysis in Section III provides useful insight into the mechanism of variable resonant frequencies and the associated tunable range under idealized conditions. This section will consider a specific implementation of the VSCA and extend the previous analysis to account for parasitic dynamics including additional mass, damping, and compliance of the stroke limiter for the PZT-based cell design. An image of the PZT-based cell (without the stroke limiter) is given in Fig. 1(b). Each cell has a 20-N blocking force and 1.5 mm free displacement.

A. Single-Cell Dynamic Model

A detailed lumped-parameter model for the specific PZT-based VSCA cell is shown in Fig. 12 for the ith cell in a strand. This model is a necessary extension of the idealized model because it includes the parasitic effects of stroke-limiter mass, stroke-limiter stiffness, and flexure damping that are present in the implemented system. Moreover, the new detailed model allows for a straightforward translation from the actual cell construction to the lumped-parameter representation. The stroke-limiter mass is lumped in to the element m, while the finite stroke-limiter stiffness is given by K. The flexure stiffness is spatially divided into two springs of equal value $2k$ on each side of the large suspended mass M. The stiffness $2k$ does vary slightly with displacement, but this variation is assumed to be small for the purpose of model development. The damping effects of the flexures are assumed to be viscous in nature and modeled using a dashpot with a constant value of b. The damping of the flexures as well as any damping in the load will shift the resonant frequencies away from their undamped counterparts. However, this shift is small, provided that b is relatively small. The PZT-generated force at the output of the second layer is now denoted by $f_{p,i}$.

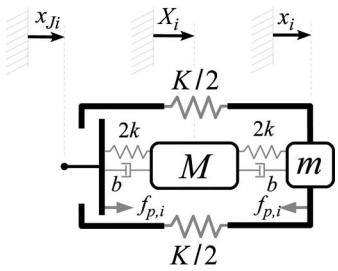

Fig. 12. Single-cell model that includes the parasitic effects of the mass m and stiffness K in the stroke-limiting beam as well as flexure damping b.

Each cell requires three generalized coordinates to describe its configuration with respect to an inertial reference frame. The first coordinate x_i determines the position of the stroke-limiter mass. The second coordinate X_i determines the position of the second-layer unit suspended mass. The third coordinate x_{Ji} determines the location of the output node junction. Note that if another cell is connected to the output node, then $x_{Ji} = x_{i-1}$.

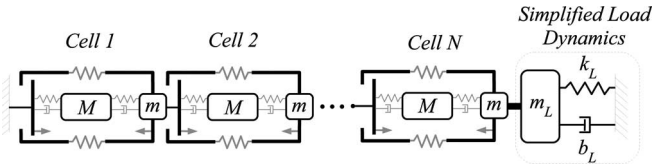

Fig. 13. Model of an assembled strand of PZT-driven cellular units connected to a general spring–mass–damper load.

TABLE II
MODEL PARAMETERS

Parameter	Value	Units
k	16.2	$\frac{N}{mm}$
K	80.1	$\frac{N}{mm}$
b	0.62	$\frac{N \cdot s}{mm}$
m	2.5	g
M	26.0	g
κ	15×10^{-3}	$\frac{C}{m}$
m_L	21.9	g
k_L	0.23	$\frac{N}{mm}$
b_L	$\approx b = 0.62$	$\frac{N \cdot s}{mm}$

B. Assembled System Behavior

Consider an arbitrary strand of cells having length N, as shown in Fig. 13. The strand is connected to a load mass m_L, which is further connected to ground through a parallel arrangement of a spring and dashpot having values of k_L and b_L. The arrangement depicted in Fig. 13 represents the usage of the actuator described in Section V.

Within the actuator, each cellular unit behaves according to the lumped model in Fig. 12. For the low frequency or static behavior, mass and damping in the dynamic model may be neglected, yielding a series compliance of

$$c_S(n, N) = \frac{n}{k} + \frac{(N-n)}{K+k} \tag{36}$$

where the first term is consistent with the idealized model in (1) and the second term accounts for the finite stiffness of the stroke-limiting beams.

If the effects of mass and damping are included, then the dynamic model for a serial chain of units, as well as the dynamic models presented in [20] and [21], can be written in the standard vibratory form as follows:

$$\mathbf{M}\ddot{\mathbf{q}} + \mathbf{B}\dot{\mathbf{q}} + \mathbf{K}(t)\mathbf{q} = \mathbf{Q}(t). \tag{37}$$

The vector $\mathbf{q}$ contains the generalized coordinates of the strand, while the vector $\mathbf{Q}(t)$ contains the piezoelectrically generated forces $f_{p,i}(t)$ acting within each cell. For simplicity, these forces are taken as the voltage applied to the cell $V_{\mathrm{PZT},i}$, scaled by an constant electromechanical transduction factor κ [21].

The parameters of the physical system used in the theoretical model are given in Table II. The stiffness parameters were taken from finite-element simulation, while the transduction constant κ was obtained from the dc response of the assembled system described in Section V. As is standard practice in vibration models, the damping b was used as a free parameter. Therefore, the damping constant b was tuned to match the experimentally observed resonant peak amplitudes.

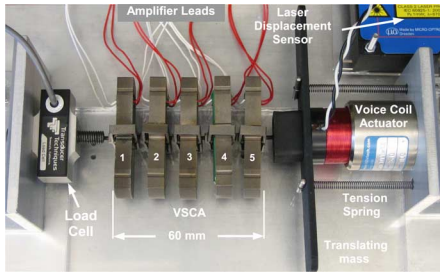

Fig. 14. Experimental apparatus for measuring static and dynamic properties of a five-cell system.

C. Cell-Switching Conditions

One important requirement for the implementation of the PZT-based VSCA system is that the combination of load and driving conditions allows the cells to turn ON or OFF without making inadvertent state transitions. The condition for turning a cell ON may be stated in terms of the applied voltage as follows:

$$V_{\min} \leq V_{\mathrm{PZT}} \leq V_{\max} \tag{38}$$

where $V_{\max}$ is the maximum voltage as specified by the material manufacturer, and $V_{\min}$ is taken as the maximum value of the time-varying voltage $V_{\mathrm{switch}}(t)$, where switching from ON to OFF first occurs

$$V_{\min} = \max_{0 \leq t \leq T} V_{\mathrm{switch}}(t). \tag{39}$$

Note from (39) that the minimum voltage is selected for a given usage duration T. Note also that $V_{\mathrm{switch}}(t)$ arises from the time-varying forces at the cell–cell connection points. The minimum ON voltage is reduced when the transduction constant κ is increased or the overall preload tension in the strand is decreased.

V. EXPERIMENTAL RESULTS

A. Static Stiffness Tunability

To demonstrate that the static tunability obeys (36), the stiffness of a serial chain having $N = 5$ was measured using the experimental apparatus shown in Fig. 14. With $N = 5$, there are $2^5 = 32$ possible arrangements of ON–OFF units. As shown in Fig. 14, the serial chain was connected to a voice coil actuator and preload tension springs. Units were turned ON or OFF by applying voltages of 150 and 0 V, respectively. Voltages were generated using a Cedrat CA-45 amplifier. The ON–OFF switching was performed with a manual switchboard. With the voice coil actuator, a 1-N peak–peak sinusoidal force was applied at 0.5 Hz about the preload force of 8 N. In general, some preload force is necessary to ensure that the units remain OFF when they receive a zero voltage input, and that nonlongitudinal vibration

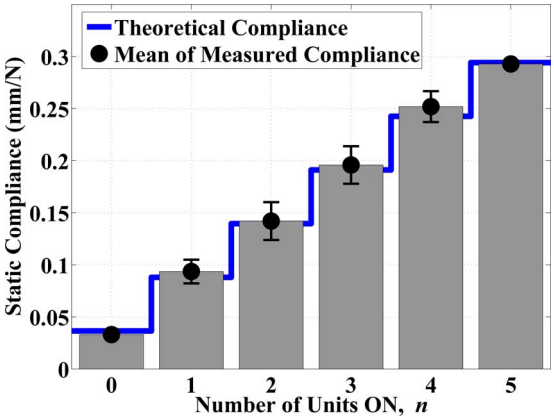

Fig. 15. Experimentally measured compliance compared with the predicted values based on theoretical stiffness.

modes remain at high frequencies. Forces were measured using a Transducer Techniques load cell, while strand displacements were measured using a MicroEpsilon laser displacement sensor. All measured signals were sampled at 1 kHz with a National Instruments data-acquisition board.

The results for the static experiment are shown in Fig. 15. For each n, there were $\binom{N}{n}$ measured data points. Each compliance data point was generated from a least squares fit to the force versus displacement data. According to (36), the equivalent series compliance is constant for a fixed value of n. However, in the real system, there are variations in the series compliance for a given n due to individual cell differences. The mean and standard deviations of the measured data were computed for each value of n. In Fig. 15, the mean is indicated by a circle, while the vertical bars represent one standard deviation about the mean. The solid staircase line is the predicted compliance based on (36). The main cell–cell difference occurs in the slight dimensional variation of the second-layer flexure angle, which can have a notable influence on the stiffness k. Other causes of stiffness variation are the slight geometric nonlinearity of the flexure and the variation in ON versus OFF stiffness of the PZT stacks. Despite these sources of variation, the mode l and the data agree well over the entire range of ON–OFF cases, and both illustrate the large tunable range for static compliance. For the experimentally considered case of $N = 5$, the compliance tunability computed from (34) is over 350%.

B. Resonant Frequency Tunability

This experimental section reinforces and illustrates the theoretical concepts developed in Sections III and IV. Frequency response tests were conducted for a VSCA with $N = 3$. The case with $N = 3$ units provides $2^3 - 1 = 7$ possible cases that can be clearly illustrated on frequency response plots. The experimental apparatus is the same as that shown in Fig. 14 only oriented so that gravity is acting along the strand.

A chirp voltage input was used to obtain the frequency response characteristics of the actuator. The chirp signal ranged from 5 to 150 Hz and contained a dc offset of 145 V to assure that the conditions in (38) were satisfied. The peak-to-peak voltage amplitude was 10 V.

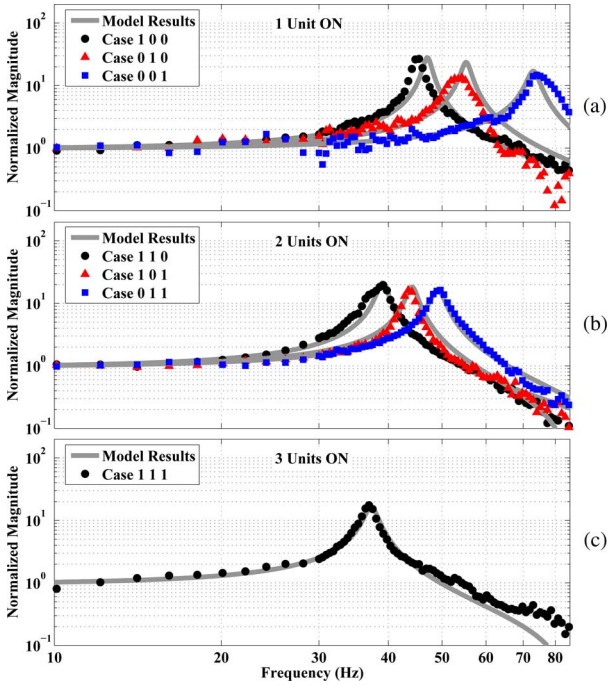

Fig. 16. Experimental results demonstrating the variable resonance concept for three serially connected units. (a) Cases with one unit ON. (b) Cases with two units ON. (c) Cases with all three units ON.

The theoretical and experimental models are compared in Fig. 16 for all of the seven possible cases. Each case is given a binary number, where the most significant bit denotes the unit connected to ground and the least significant bit denotes the unit connected to the load. The gain in the frequency response is normalized with respect to the dc displacement. Therefore, the vertical axes in Fig. 16 represent the frequency-dependent amplification of displacement. The average measured amplification at the fundamental resonance was 17.8 with a standard deviation of 4.4. When comparing the fundamental frequency location between the model and the experimental results, the coefficient of determination is very high ($R^2 = 0.993$) for the entire tuning range of nearly 38 Hz.

For the loaded strand, the load mass and stiffness ratios can be computed from the parameters in Table II as $\gamma_m = 21.9/26.0 = 0.84$ and $\gamma_k = 0.23/16.2 = 0.014$. From Fig. 11 for the case with $N = 3$, the tunability as predicted by the idealized model is over 100%. Furthermore, as indicated by theoretical propositions, the lowest fundamental frequency ($\Sigma_{\min} = 37.5$ Hz) was obtained in the [1 1 1] case, while the highest fundamental resonant frequency ($\sigma_{\max,\text{first}}(1) = 75.2$ Hz) was obtained was in the [0 0 1] case. The computation of the dynamic tunability from (35) yields a value of over 100%, which agrees well with the idealized model.

C. Discussion

The experimental results presented in this section illustrate three key features of the VSCA approach.

1) The VSCA approach allows for a wide tunability of both the static stiffness and the first resonant peak in an assembled system. For the experimental system having only $N = 3$ units, the tunability exceeds 100%. The tunability is also increased as N becomes larger and as higher modes are excited.
2) The results show the high degree of dynamic displacement amplification (≥ 5) when there is low damping in the system. Hence, the preexisting large static amplification produced by the nested flexures is augmented in the VSCA approach such that resonant peaks occur over a wide range of frequencies useful for robotic locomotion and manipulation.
3) The experimental results and the model prediction are in close agreement for nearly all cases tested. The small model residuals, especially near resonance, validate linearity assumptions and demonstrate a sound model for the dominant energy storage and dissipation modes in the driven system.

VI. Conclusion

This paper presented two main contributions: 1) quantification of the essential theoretical properties of VSCAs; and 2) the implementation and testing of a novel PZT-based VSCA design. The change in both stiffness and resonant frequencies is achieved by selectively turning variable stiffness units ON or OFF within a serial strand. Experiments and models illustrate the shift in resonant frequency based on a simple change in ON–OFF configuration.

The PZT-based actuators considered in this paper will be valuable in many biorobotics applications because they achieve static strain that is commensurate with skeletal muscle (10%–20%) and their strain is further amplified under resonance conditions. Furthermore, VSCA designs based on PZT actuator cells are durable, low power, and high-bandwidth devices. One particular advantage of PZT is its near-zero power consumption when holding a load in dc.

The tunability of the PZT actuator also holds particular promise as an energy harvesting device. Harvesting devices that vary resonant frequency do exist (e.g., [27], [28]), but such systems require an additional actuator to tune the resonant frequency. The cellular PZT system described in this paper provides a means for easily tuning resonance over a wide range in real time without the use of additional actuators. This may be very advantageous for mobile robots capable of passively gathering energy from their environment (e.g., fish robots within a flow).

Our group is presently exploring application areas for our VSCA technology include deep-sea robotics and nuclear-reactor-inspection robots. Further extensions of the technology include using cells with differing stiffnesses to achieve more uniform modal density across the tuning range. The theoretical treatment may also be extended to include parallel and antagonistic strands. Overall, the ongoing development of this actuator is expected to create opportunities for utilizing both variable stiffness and variable resonance actuation in robotics applications.

Appendix

Proof of Lemma 2: Suppose that Lemma 2 is not true, i.e., there exist positive integers $l'_1, l'_2, \ldots, l'_n$ such that $J(l'_1, l'_2, \ldots, l'_n) > J(1, 1, \ldots, 1, N-n+1)$. Then, this implies

$$l'_1 x_1^2 + l'_2 x_2^2 + \cdots + l'_{n-1} x_{n-1}^2 + l'_n x_n^2 > x_1^2 + x_2^2 + \cdots + x_{n-1}^2 + (N-n+1)x_n^2. \quad \text{(A1)}$$

Using the constraint $l'_n = N - p - \sum_{i=1}^{n-1} l'_i$ allows (A1) to be rewritten as follows:

$$\left(\frac{l'_1 - 1}{1 - n + p + \sum_{i=1}^{n-1} l'_i}\right)\left(\frac{x_1}{x_n}\right)^2 + \cdots + \left(\frac{l'_{n-1} - 1}{1 - n + p + \sum_{i=1}^{n-1} l'_i}\right)\left(\frac{x_{n-1}}{x_n}\right)^2 > 1. \quad \text{(A2)}$$

The aforementioned inequality can be more strictly stated as follows:

$$\left(\frac{1 - n + \sum_{i=1}^{n-1} l'_i}{1 - n + p + \sum_{i=1}^{n-1} l'_i}\right)\left(\frac{x_{n-1}}{x_n}\right)^2 > 1 \quad \text{(A3)}$$

which is a contradiction because of (15). ■

References

[1] R. Schiavi, G. Grioli, S. Sen, and A. Bicchi, "VSA-II: A novel prototype of variable stiffness actuator for safe and performing robots interacting with humans," in *Proc. IEEE Int. Conf. Robot. Autom.*, 2008, pp. 2171–2176.

[2] N. Hogan, "Impedance control: An approach to manipulation—Part I: Theory," *Trans. Amer. Assoc. Mech. Eng. J. Dyn. Syst., Meas. Control*, vol. 107, no. 1, pp. 1–7, 1985.

[3] H. Hanafusa and H. Asada, "A robotic hand with elastic fingers and its application to assembly processes," in *Proc. FAC Symp. Inf. Control Probl. Prod. Eng.*, 1977, pp. 127–138.

[4] H. Hanafusa and H. Asada, "Stable pretension by a robotic hand with elastic fingers," in *Proc. 7th Int. Symp. Ind. Robots*, 1977, pp. 361–367.

[5] G. A. Pratt and M. M. Williamson, "Series elastic actuators," in *Proc. IEEE Int. Conf. Intell. Robots Syst.*, 1995, vol. 1, pp. 399–406.

[6] S. K. Au and H. M. Herr, "Powered ankle-foot prosthesis," *IEEE Robot. Autom. Mag.*, vol. 15, no. 3, pp. 52–59, Sep. 2008.

[7] J. Choi, S. Park, W. Lee, and S.-C. Kang, "Design of a robot joint with variable stiffness," in *Proc. IEEE Int. Conf. Robot. Autom.*, 2008, pp. 1760–1765.

[8] R. Van Ham, B. Vanderborght, M. Van Damme, B. Verrelst, and D. Lefeber, "MACCEPA, the mechanically adjustable compliance and controllable equilibrium position actuator: Design and implementation in a biped robot," *Robot. Auton. Syst.*, vol. 55, no. 10, pp. 761–768, 2007.

[9] A. Albu-Schaffer, O. Eiberger, M. Grebenstein, S. Haddadin, C. Ott, T. Wimbock, S. Wolf, and G. Hirzinger, "Soft robotics," *IEEE Robot. Autom. Mag.*, vol. 15, no. 3, pp. 20–30, Sep. 2008.

[10] M. H. Raibert, *Legged Robots That Balance*. Cambridge, MA: MIT Press, 1986.

[11] J. Hurst and A. Rizzi, "Series compliance for an efficient running gait," *IEEE Robot. Autom. Mag.*, vol. 15, no. 3, pp. 42–51, Sep. 2008.

[12] K. K. Issac and S. K. Agrawal, "An investigation into the use of springs and wing motions to minimize the power expended by a pigeon-sized mechanical bird for steady flight," *Trans. Amer. Assoc. Mech. Eng. J. Mech. Des.*, vol. 129, no. 4, pp. 381–389, 2007.

[13] J. Yan, R. Wood, S. Avadhanula, M. Sitti, and R. Fearing, "Towards flapping wing control for a micromechanical flying insect," in *Proc. IEEE Int. Conf. Robot. Autom.*, 2001, vol. 4, pp. 3901–3908.

[14] P. Valdivia y Alvarado and K. Youcef-Toumi, "Design of machines with compliant bodies for biomimetic locomotion in liquid environments," *Trans. Amer. Assoc. Mech. Eng. J. Dyn. Syst., Meas. Control*, vol. 128, no. 1, pp. 3–13, 2006.
[15] M. Uemura, K. Kanaoka, and S. Kawamura, "A new control method utilizing stiffness adjustment of mechanical elastic elements for serial link systems," in *Proc. IEEE Int. Conf. Robot. Autom.*, 2007, pp. 1437–1442.
[16] N. Lobontiu, M. Goldfarb, and E. Garcia, "Maximizing the resonant displacement of piezoelectric beams," in *Proc. SPIE Int. Soc. Opt. Eng.*, vol. 3668, no. I, pp. 154–163, 1999.
[17] R. Kornbluh, R. Pelrine, J. Eckerle, and J. Joseph, "Electrostrictive polymer artificial muscle actuators," in *Proc. IEEE Int. Conf. Robot. Autom.*, 1998, vol. 3, pp. 2147–2154.
[18] K.-J. Cho and H. Asada, "Architecture design of a multiaxis cellular actuator array using segmented binary control of shape memory alloy," *IEEE Trans. Robot.*, vol. 22, no. 4, pp. 831–843, Aug. 2006.
[19] L. Odhner and H. Asada, "Equilibrium point control of artificial muscles using recruitment of many motor units," in *Proc. 2nd Biennial IEEE/RAS-EMBS Int. Conf. Biomed. Robot. Biomechatronics, BioRob*, 2008, pp. 121–126.
[20] T. W. Secord and H. H. Asada, "A variable stiffness PZT cellular actuator with tunable resonance for cyclic motion tasks," in *Proc. IEEE Int. Conf. Robot. Autom.*, 2009, pp. 176–181.
[21] T. W. Secord and H. H. Asada, "Cellular muscle actuators with variable resonant frequencies," *Robotics Sci. Syst.*, to be published.
[22] J. Ueda, T. Secord, and H. H. Asada, "Design of PZT cellular actuators with power-law strain amplification," in *Proc. IEEE Int. Conf. Intell. Robots Syst.*, 2007, pp. 1160–1165.
[23] N. Hogan, "Adaptive control of mechanical impedance by coactivation of antagonist muscles," *IEEE Trans. Autom. Control*, vol. AC-29, no. 8, pp. 681–690, Aug. 1984.
[24] G. Gladwell, *Inverse Problems in Vibration*. Dordrecht, The Netherlands: Martinus Nijhoff, 1986.
[25] K. Bathe, *Finite Element Procedures*. Upper Saddle River, NJ: Prentice-Hall, 1996.
[26] F. Gantmacher and M. Krein, *Oscillation Matrices*, revised ed. Washington, DC: Amer. Math. Soc., 2002.
[27] E. S. Leland and P. K. Wright, "Resonance tuning of piezoelectric vibration energy scavenging generators using compressive axial preload," *Smart Mater. Struct.*, vol. 15, no. 5, pp. 1413–1420, 2006.
[28] V. R. Challa, M. Prasad, Y. Shi, and F. T. Fisher, "A vibration energy harvesting device with bidirectional resonance frequency tunability," *Smart Mater. Struct.*, vol. 17, no. 1, pp. 015035-1–015035-10, 2008.

Thomas W. Secord (M'10) received the B.S. degree in mechanical engineering from the University of Minnesota, Minneapolis, in 2005 and the M.S. degree in mechanical engineering in 2007 from the Massachusetts Institute of Technology, Cambridge, where he is currently working toward the Ph.D. degree.

His research interests include robotics and control, mechatronics, artificial muscles, and actuator systems using smart materials.

H. Harry Asada (A'85–M'06) received the B.S. degree in mechanical engineering in 1973 and the M.S. and Ph.D. degrees in precision engineering from Kyoto University, Kyoto, Japan, in 1975 and 1978, respectively.

He was a Research Scientist with the Robotics Institute of Carnegie Mellon University, Pittsburgh, PA, prior to joining the Massachusetts Institute of Technology (MIT), Cambridge, as a Faculty Member in 1982. From 1985 to 1988, he held a faculty position with the Department of Applied Mathematics and Physics, Kyoto University. Since 1990, he has been a Full Professor with the Department of Mechanical Engineering, MIT. He specializes in robotics and control, and his research interests include biomedical engineering, system dynamics, engineering design, manufacturing, and communication systems.

Prof. Asada was the recipient of the O. Hugo Shuck Best Paper Award from the American Control Council in 1984, three Best Paper Awards at the IEEE Robotics and Automation Conference in 1993, 1997, and 1999, and five Best Journal Papers from the *Journal of Advanced Robotics*, the *Journal of Instrument and Control Engineering*, and the *Journal of Dynamic Systems, Measurement, and Control*. He is also the recipient of the 1998 American Society of Mechanical Engineers (ASME) Dynamic Systems and Control Outstanding Researcher Award. He is a Fellow of ASME.